Full length article

Local order in high-entropy alloys and associated deuterides – a total scattering and Reverse Monte Carlo study

Magnus M. Nygård [a], Wojciech A. Sławiński [b], Gustav Ek [c], Magnus H. Sørby [a,*],
Martin Sahlberg [c], David A. Keen [d], Bjørn C. Hauback [a]

[a] *Institute for Energy Technology, Department for Neutron Materials Characterization, P.O. Box 40, Kjeller NO-2027, Norway*
[b] *University of Warsaw, Faculty of Chemistry, Pasteura 1, Warsaw PL-02-093, Poland*
[c] *Uppsala University, Department of Chemistry – Ångström Laboratory, Box 523, Uppsala, SE-75120, Sweden*
[d] *ISIS Facility, Rutherford Appleton Laboratory, Harwell Campus, Didcot, Oxfordshire OX11 0QX, United Kingdom*

ARTICLE INFO

ABSTRACT

Many of the materials properties of high-entropy alloys (HEAs), like increased hardness, reduced thermal and electrical conductivity, and interesting hydrogen storage properties, are proposed to be related to local lattice distortions of the crystal structure due to the significant size differences between the elements of the alloy. However, direct evidence of this effect is very limited in the literature, and it therefore remains a hypothesis. This work presents a detailed assessment of the local lattice distortion in three body-centered cubic (bcc) HEAs TiVNb, TiVZrNb and TiVZrNbHf with varying atomic size differences using total scattering measurements and Reverse Monte Carlo structure modelling. The analysis indicates that the amount of local lattice distortion in the alloys increases with the elemental size difference in the alloy. The amount of lattice distortion is relieved when dideuterides with CaF_2-type structures ($Fm\overline{3}m$) are formed from the bcc ($Im\overline{3}m$) HEAs. Analyses of the local environments around the deuterium atoms reveal an interesting correlation between the valence-electron concentration (VEC) of the nearest-neighbour metals and the stability of tetrahedral interstices with respect to deuterium occupation. Moreover, there is a tendency towards Ti/Nb short-range order in $TiVNbD_{5.7}$ where the mixing entropy is lowest. In $TiVZrNbHfD_{10}$, about 6 % of the deuterium atoms are displaced from the tetrahedral interstices with smaller volumes to octahedral interstices.

1. Introduction

The signature of high-entropy alloys (HEAs) is the formation of a single-phase solid solution from multiple principal elements in a nearly equimolar mixture. The crystalline structures of these materials are often simple, *e.g.*, body-centered cubic (bcc) and cubic close-packed (ccp), and as a consequence the elements are randomly distributed over a single crystallographic site. Thus, HEAs are significantly disordered materials and it has been suggested that the simple structures are stabilized by a large entropy of mixing. Recently, HEAs have attracted much scientific attention due to their interesting materials properties that are often remarkably different compared to more conventional alloys [1–3]. However, the core principles from which these properties are usually attributed still remains hypothetical [4]. For instance, when there is an ap-

preciable size difference between the elements it seems reasonable that there must be local lattice distortions [5,6]. It has been suggested that this effect is more severe in HEAs than in compositionally less complex alloys [2,7,8]. A simple measure that is often used to indicate the amount of lattice distortion is

$$\delta r = \sqrt{\sum_{i=1}^{N} c_i \left(1 - \frac{r_i}{\overline{r}}\right)^2} \cdot 100\% \qquad (1)$$

where $\overline{r} = \sum_{i=1}^{N} c_i r_i$ with $\{c_i\}_{i=1}^{N}$ and $\{r_i\}_{i=1}^{N}$ as the concentrations and radii of the N chemical species in the HEA, respectively. In the present work the atomic radii given in Table 1 are used. Indeed, many exceptional materials properties have been attributed to this *lattice distortion effect*. Notable examples include greater mechanical strength, exceptional toughness at cryogenic temperatures, increased thermal and electrical resistivity and superior hydrogen storage properties [2–4]. Still, it remains an open challenge to obtain direct experimental evidence of the expected larger distortions in HEAs as compared to conventional alloys. The reason for this is

Table 1
Valence-electron concentrations *VEC* and atomic radii for a selection of elements. All values are adopted from Ref. [2].

Element	VEC [∅]	r [Å]
Ti	4	1.46
V	5	1.32
Cr	6	1.25
Mn	7	1.35
Fe	8	1.24
Co	9	1.25
Ni	10	1.25
Zr	4	1.60
Nb	5	1.43
Hf	4	1.58

related to the difficulty of obtaining a detailed assessment of the local structure [9].

In this context, total scattering is one of the viable options for probing the local structure. This is a technique that extends regular diffraction and involves additional measurements to obtain an accurate assessment of both the Bragg and diffuse scattering from the sample. The sum of these components is known as the total scattering structure factor $F(Q)$. Analysis is often performed with the Fourier transform of this function known as the pair-distribution function (PDF) $G(r)$ defined as

$$G(r) = \sum_{i=1}^{N} \sum_{j=1}^{N} c_i c_j \bar{b}_i \bar{b}_j \left[g_{ij}(r) - 1 \right] \qquad (2)$$

where $\{c_i\}_{i=1}^{N}$ and $\{\bar{b}_i\}_{i=1}^{N}$ are the concentrations and neutron scattering lengths of the N distinct chemical species within the scattering system, respectively. $g_{ij}(r)$ are the partial PDFs defined as

$$g_{ij}(r) = \frac{1}{\rho_j} \frac{n_{ij}(r)}{4\pi r^2 dr} \qquad (3)$$

where $\rho_j = c_j \rho_0$ is the number density of species j and $n_{ij}(r)$ is the number of chemical species j at distances between r and $r + dr$ from a chemical species of type i. Thus, the PDF is a weighted histogram of the interatomic distances in the material. In these functions, the lattice distortion is directly observable as broadening and positional shifts of the peaks in the PDF.

A few studies have explored the local structures of HEAs from a total scattering perspective [10–12]. In these studies, the average structure is generally able to explain most observed features in the PDFs, but at $r < 4$ Å there are often significant deviations [10,11]. The effect is especially clear if larger elements, such as Zr and Hf, are incorporated into the HEA. These publications demonstrate the presence of the effect, but they are unable to quantify its extent. The first quantitative assessment of the lattice strain in a HEA was reported for CrMnFeCoNi [12]. In this work, the peaks corresponding to the first six coordination shells in the PDF were fitted by Gaussian functions, and their full widths at half maximum (FWHM) were compared with those obtained for five related, but compositionally simpler, compounds. It was found that the lattice distortion in the HEA was not anomalously large compared to the other materials. However, the elements in CrMnFeCoNi have similar sizes as is reflected by $\delta r = 3.24$ %.

The present work aims to address whether the amount of lattice distortion intensifies with increasing spread in atom sizes. A quantitative assessment is obtained from Reverse Monte Carlo (RMC) structure modelling to total scattering measurements of three HEAs with varying atomic size differences, TiVNb ($\delta r = 4.29$ %), TiVZrNb ($\delta r = 6.87$ %) and TiVZrNbHf ($\delta r = 6.96$ %). These alloys also exhibit interesting hydrogen storage properties [13–16].

In particular, the hydrogen content in TiVZrNbHf has been reported to reach $[H]/[M] = 2.5$ [13]. This is much higher than in the binary hydrides formed from its constituents and suggests that both tetrahedral and octahedral interstices are substantially occupied simultaneously. This is not common for interstitial hydrides. Moreover, hydrides formed from HEAs containing large amounts of Zr and Hf have been observed to phase separate under hydrogen desorption [15,16]. Therefore, we also hope to understand whether there are explanations for this interesting behaviour hidden in the local structure.

2. Experimental

Two 15 g samples for each of the nominal compositions TiVNb, TiVZrNb and TiVZrNbHf were synthesised by melting lumps of Ti (Kurt J. Lesker, 99.99 % metals basis), V (ChemPUR, 99.9 % metals basis), Nb (Alfa Aesar, 99.5 %), Zr (Goodfellow, 99.2 % (max 0.8 % Hf) metals basis) and Hf (ChemPUR 99.8 %, metals basis) in an electric arc furnace under Ar atmosphere. The samples were turned and remelted five times to enhance homogeneity. The mass losses were in all cases less than 0.1 wt%, and thus the resultant composition can be considered as very close to the nominal. For each composition, one sample was filed to a powder using a metal file. The second sample was cut into smaller pieces, placed inside an autoclave and connected to a Sieverts apparatus. The autoclave was evacuated and heated to 340 °C for 2 h. It was then exposed to deuterium gas (^{2}H, purity 99.7 %, Air Liquide) at 40 bar until there was no observable change in the gas pressure. The final deuterium contents were determined thermogravimetrically by heating the obtained deuterides in a heat-flux type Netzsch STA 449 F3 Jupiter apparatus under flowing Ar at 50 mL/min. The compositions were determined as $TiVNbD_{5.7}$, $TiVZrNbD_8$ and $TiVZrNbHfD_{10}$. Deuterium was used instead of hydrogen to limit the level of incoherent scattering in the neutron total scattering measurements.

The obtained alloys and deuterides were sealed inside 0.5 mm borosilicate glass capillaries and 5.9 mm inner diameter V containers for the X-ray and neutron total scattering measurements, respectively. The combination of these probes was necessary to obtain sufficient contrast between all the elements. The X-ray total scattering measurements were performed at the Swiss-Norwegian beamline (SNBL) BM31 at the European Synchrotron Radiation Facility (ESRF) in Grenoble, France. The data was collected using a CMOS DEXELA 2D detector [17] with an X-ray wavelength of 0.3171 Å. Background subtraction and data correction was done using the program GudrunX [18] to obtain the total scattering functions $F(Q)$, $G(r)$ and $D(r)$ as defined in Ref. [19]. The neutron total scattering measurements were carried out at the GEM diffractometer at ISIS Neutron and Muon Source, Rutherford Appleton Laboratory, United Kingdom [20]. Each sample was measured at room temperature (*RT*) for 10 h by five detector banks centred on scattering angles 154.4°, 91.3°, 63.9°, 35° and 18°. The data used for the Rietveld refinements were generated for each detector bank by Mantid [21]. Measurements were also carried out for an empty V container, a V-5.14%Nb rod and the empty instrument to allow background subtraction and data correction to be performed by standard means using the program GudrunN [18]. Final corrections to the obtained X-ray and neutron $F(Q)$, $G(r)$ and $D(r)$ were done in the program StoG distributed alongside the RMCProfile software [22].

Rietveld refinements were performed with the software GSAS coupled with the graphical user interface EXPGUI [23,24]. The structures were refined against synchrotron radiation powder X-ray diffraction (SR-PXD) and powder neutron diffraction (PND) patterns simultaneously. The peak shapes were modelled by Thompson–Cox–Hastings pseudo-Voigt functions in the SR-PXD patterns [25]. The corresponding peaks in the PND patterns were modelled by a convolution of a pseudo-Voigt function with the

Ikeda–Carpenter function [26]. In both cases the backgrounds were modelled with a 12th order shifted-Chebyshev polynomial.

The RMC modelling was done with the development version of the RMCProfile v7 software which will replace the current RM-CProfile v6 [22]. The structures of the alloys were modelled using supercells of $19 \times 19 \times 19$ unit cells containing 13,718 atoms. This enabled us to calculate the PDFs $G(r)$ and $D(r)$ up to 30 Å. To cover the same length scale in the corresponding deuterides supercells made from $14 \times 14 \times 14$ unit cells with 32,928 atoms were used. A total of four functions were fitted for each probe, $F(Q)$, $G(r)$, $D(r)$ and the Bragg peak intensities, respectively. Thus, the model was fitted to a total of eight functions simultaneously. The relative weighting of the different functions was determined by trial and error to ensure that the model was fitted well to them all. Two kinds of moves were attempted with equal probability during the modelling procedure. The first kind allows two metal atoms or a deuterium atom and a vacancy chosen at random to swap places. The second kind allows an atom selected at random to be translated a random distance. The maximum distance for translation moves was 0.10 Å.

3. Results and discussion

Fig. 1 shows simultaneous Rietveld refinements of both SR-PXD and PND patterns. The corresponding crystallographic data are shown in Tables 2 and 3 for the alloys and deuterides, respectively. From the figure it is clear that the scattering intensity of the alloys is very weak with neutrons. This is due to the opposite signs of the neutron scattering lengths of Ti/V (-3.438 fm/-0.3824 fm) and

Table 2

Crystallographic data for TiVNb, TiVZrNb and TiVZrNbHf at *RT*. Estimated standard deviations are given in parentheses.

Compound:	**TiVNb**					
Space group:	*Im$\bar{3}$m*					
Lattice parameter, a:	3.2050(2) Å					
Unit cell volume, V_0:	32.921(7) Å^3					
Mass density, ρ:	6.448 g/cm^3					
Number density, ρ_0:	0.0608 atoms/Å^3					

Atom	Site	x	y	z	U_{iso}	Occupancy
Ti	2a	0	0	0	0.0277(12)	1/3
V	2a	0	0	0	0.0014(9)	1/3
Nb	2a	0	0	0	0.0102(2)	1/3

Compound:	**TiVZrNb**					
Space group:	*Im$\bar{3}$m*					
Lattice parameter, a:	3.3067(5) Å					
Unit cell volume, V_0:	36.156(15) Å^3					
Mass density, ρ:	6.498 g/cm^3					
Number density, ρ_0:	0.0553 atoms/Å^3					

Atom	Site	x	y	z	U_{iso}	Occupancy
Ti	2a	0	0	0	0.03(2)	1/4
V	2a	0	0	0	0.05(7)	1/4
Zr	2a	0	0	0	0.02(6)	1/4
Nb	2a	0	0	0	0.02(7)	1/4

Compound:	**TiVZrNbHf**					
Space group:	*Im$\bar{3}$m*					
Lattice parameter, a:	3.36466(9) Å					
Unit cell volume, V_0:	38.091(3) Å^3					
Mass density, ρ:	8.047 g/cm^3					
Number density, ρ_0:	0.0525 atoms/Å^3					

Atom	Site	x	y	z	U_{iso}	Occupancy
Ti	2a	0	0	0	0.0496(13)	1/5
V	2a	0	0	0	0.2(2)	1/5
Zr	2a	0	0	0	0.017(4)	1/5
Nb	2a	0	0	0	0.0169(4)	1/5
Hf	2a	0	0	0	0.0172(4)	1/5

Table 3

Crystallographic data for TiVNbD$_{5.7}$, TiVZrNbD$_8$ and TiVZrNbHfD$_{10}$ at *RT*. Estimated standard deviations are given in parentheses.

Compound:	**TiVNbD$_{5.7}$**					
Space group:	*Fm$\bar{3}$m*					
Lattice parameter, a:	4.42369(9) Å					
Unit cell volume, V_0:	86.567(5) Å^3					
Mass density, ρ:	5.198 g/cm^3					
Number density, ρ_0:	0.1340 atoms/Å^3					

Atom	Site	x	y	z	U_{iso}	Occupancy
Ti	2a	0	0	0	0.00287(12)	1/3
V	2a	0	0	0	0.00175(18)	1/3
Nb	2a	0	0	0	0.00376(5)	1/3
D	8c	1/4	1/4	1/4	0.01125(4)	0.950(6)

Compound:	**TiVZrNbD$_8$**					
Space group:	*Fm$\bar{3}$m*					
Lattice parameter, a:	4.5308(2) Å					
Unit cell volume, V_0:	93.007(13) Å^3					
Mass density, ρ:	5.340 g/cm^3					
Number density, ρ_0:	0.1290 atoms/Å^3					

Atom	Site	x	y	z	U_{iso}	Occupancy
M	2a	0	0	0	0.0074(2)	1
D	8c	1/4	1/4	1/4	0.0153(1)	0.99(2)

Compound:	**TiVZrNbHfD$_{10}$**					
Space group:	*Fm$\bar{3}$m*					
Lattice parameter, a:	4.57324(6) Å					
Unit cell volume, V_0:	95.647(4) Å^3					
Mass density, ρ:	6.689 g/cm^3					
Number density, ρ_0:	0.1255 atoms/Å^3					

Atom	Site	x	y	z	U_{iso}	Occupancy
M	2a	0	0	0	0.00542(12)	1
D	4b	1/2	1/2	1/2	0.291(7)	0.120(2)
D	8c	1/4	1/4	1/4	0.01150(5)	0.940(1)

Zr/Nb/Hf (7.16 fm/ 7.054 fm/7.77 fm) [27]. Even peaks from the V-can are visible in the PND patterns since the scattering intensities from the alloys are very low. These peaks are not present in the total scattering structure factors $F(Q)$ where the scattering from the V-can has been corrected for. An Fe impurity that originates from the metal file is also present in the PND pattern of TiVZrNb. These extra peaks are not visible in the SR-PXD pattern and our Rietveld refinement indicates that the mass percentage of the impurity is less than 0.1 wt%. Thus, its contribution to the PDF should be insignificant.

The RMC fits to the X-ray and neutron $G(r)$, $D(r)$, $F(Q)$ and the Bragg peak intensities for TiVZrNb and TiVZrNbD$_8$ are shown in Figs. 2 and 3, respectively. The figures show that the obtained models correspond very well with the measured data. The RMC fits for the other alloys and deuterides are of similar quality. These fits are shown in Figs. A.1–A.4 in the supplementary information.

### 3.1. Order/disorder in the solid solutions

The degree of order in a solid solution can be characterized by the pairwise multicomponent short-range order (PM-SRO) parameters [28]. These are defined as

$$\alpha_{ij}(m) = \frac{p_{ij}(m) - c_j}{\delta_{ij} - c_j} \tag{4}$$

where c_j is the concentration of element j in the alloy, δ_{ij} is the Kronecker delta function and $p_{ij}(m)$ is the probability of observing an element of type j in the mth coordination shell surrounding an element of type i. It follows that $\sum_{j=1}^{N} p_{ij}(m) = 1$ for all the N elements in the alloy, and we note that for an equimolar HEA we have $c_j = c = 1/N$ for all elements, j. The PM-SRO parameters indicate the amount of deviation from a completely randomized solid
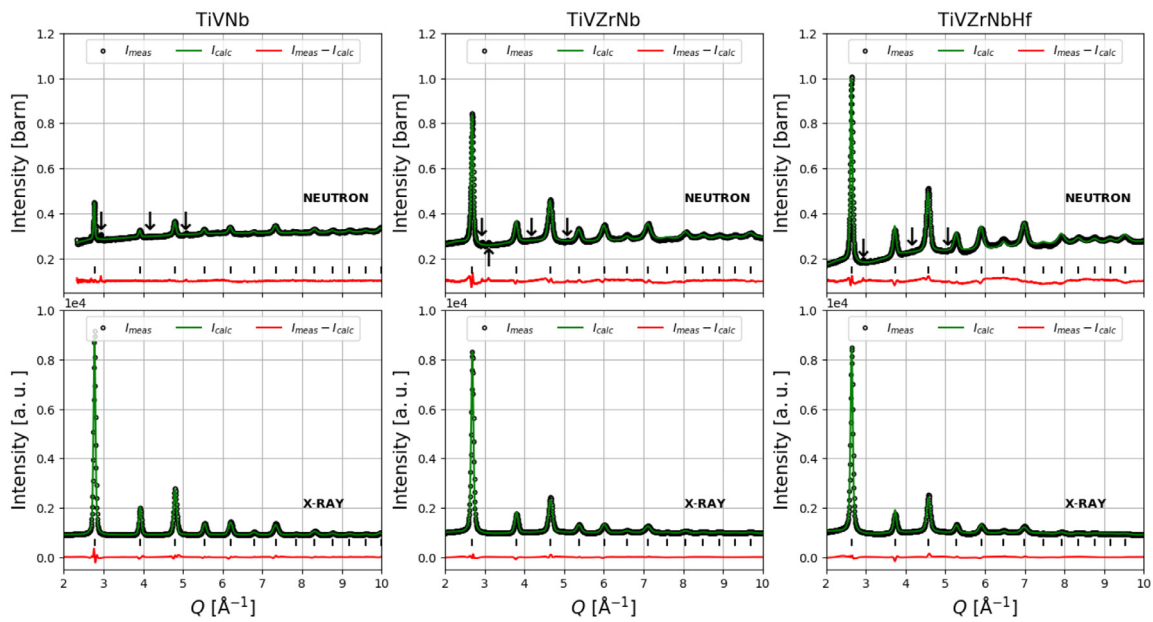
(a) Alloys.
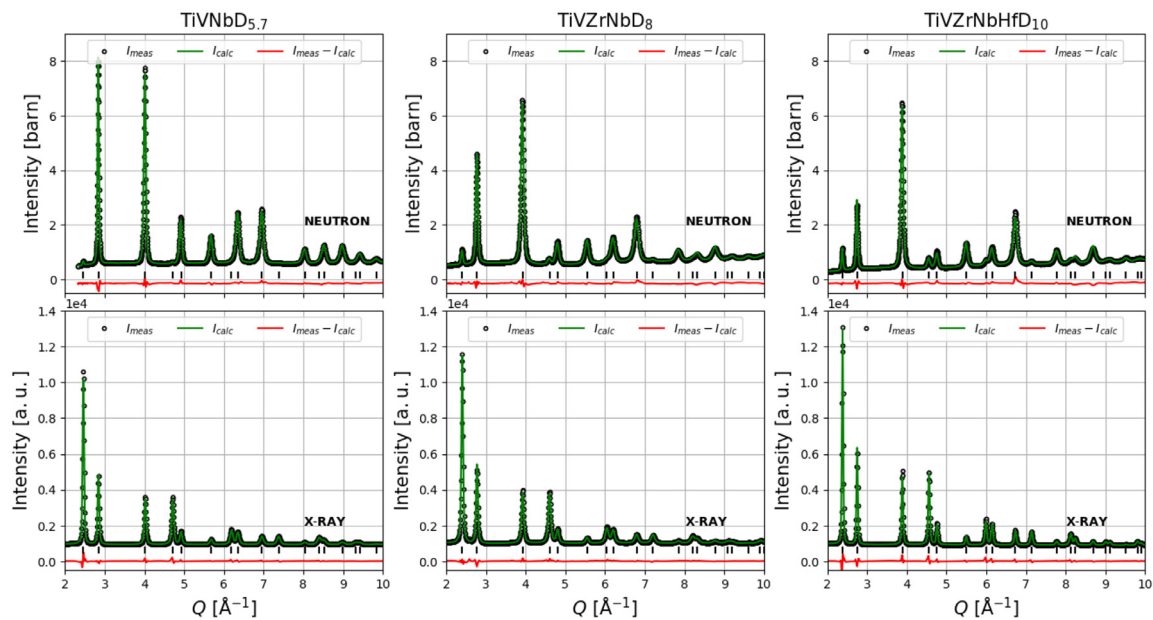
(b) Deuterides.

Fig. 1. Rietveld refinements of PND and SR-PXD patterns for TiVNb, TiVZrNb and TiVZrNbHf **(a)** and the corresponding deuterides **(b)** at *RT*. Visible peaks from the V-can and an Fe impurity are indicated by downwards and upwards pointing black arrows, respectively.

solution. $\alpha_{ii}(m) = 1$ corresponds to a scenario where the mth coordinate shell around atoms of type i only contains elements of type i. $\alpha_{ii}(m) = -1/(N-1)$ implies that there are no atoms of type i in this coordination shell. On the other hand, $\alpha_{ij}(m) = 1$ indicates that there are no atoms of type j in the mth coordination shell around a central atom of type i, and $\alpha_{ij}(m) = -(N-1)$ implies that there are only atoms of type j in this coordination shell. In any case, a completely randomized solid solution is characterized by $\alpha_{ij}(m) = 0$ for all i, j and m. The PM-SRO parameters obtained from the RMC structure models of the HEAs are shown in Fig. 4(a). It can be seen that the models are very close to randomized solid solutions. There is a somewhat higher probability for Nb to be co-

ordinated by itself in the first coordination spheres of TiVZrNb. The same is observed for Hf in TiVZrNbHf. Nevertheless, the deviations from an idealized solid solution are very subtle with respect to the limiting scenarios outlined above. Fig. 4(b) presents the PM-SRO parameters from the RMC structure models of the corresponding deuterides. For TiVZrNbD$_8$ and TiVZrNbHfD$_{10}$ the obtained values are comparable to those obtained for the alloys, but in TiVNbD$_{5.7}$ the model shows a slight tendency of short-range Ti/Nb order. In particular, there is a higher probability for Ti and Nb to be coordinated by a similar element, *i.e.*, Ti by Ti and Nb by Nb, in the 4th, 8th, 12th, 15th, 19th, 23rd, 27th, 30th and 34th coordination spheres. The probability for Ti to be coordinated by Nb, and *vice*
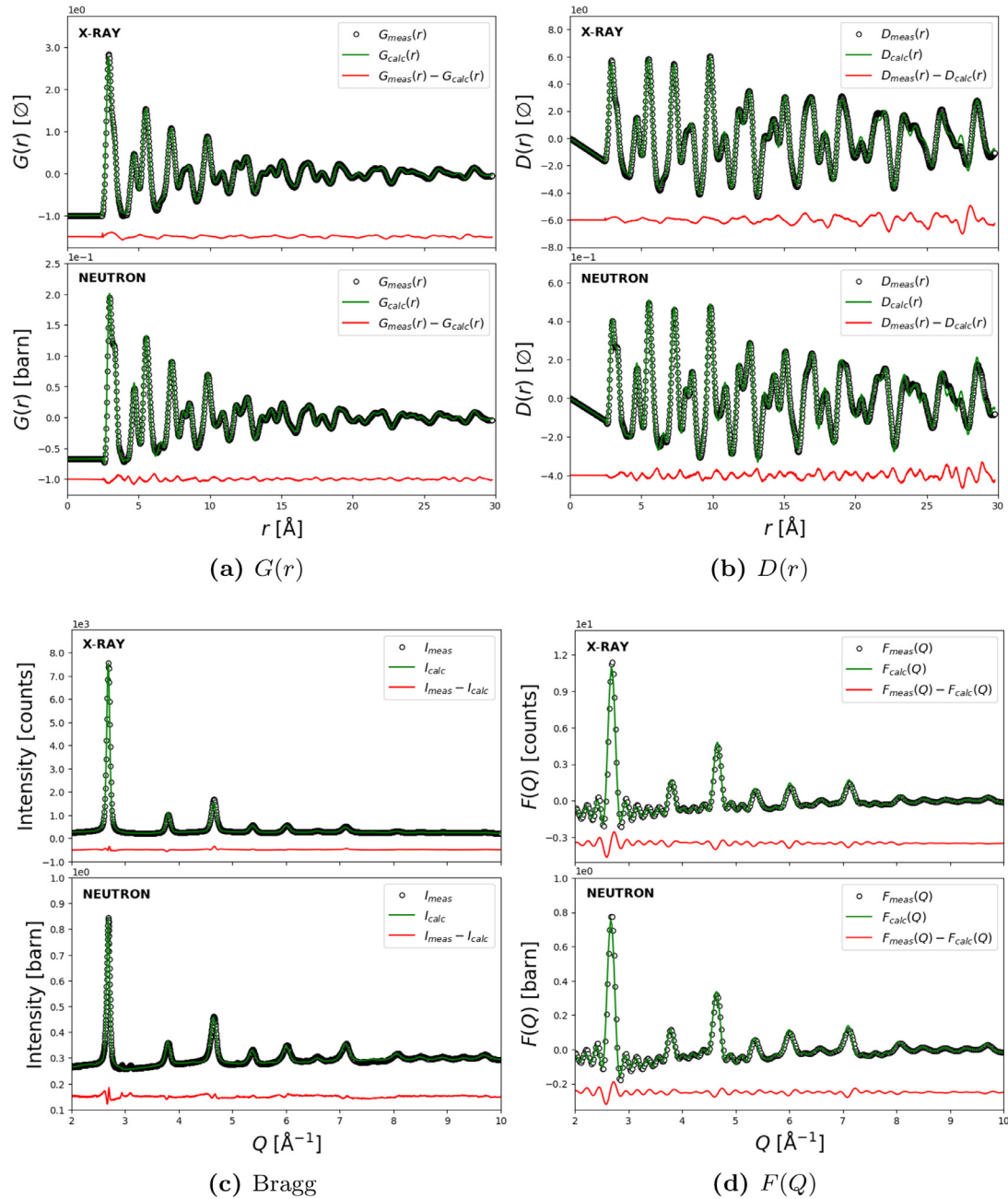
Fig. 2. RMC fits to the X-ray and neutron total scattering measurements of TiVZrNb.

versa, is reduced correspondingly. Inspection of the structure reveals that these coordination shells form a $2 \times 2 \times 2$ face-centered cubic supercell, as shown in Fig. 5. The PM-SRO parameters are far from the limiting values outlined above, and thus, indicates that the ordering is far from perfect. In particular, it does not extend beyond the 34th coordination sphere which correspond to length scales smaller than 2 nm. It is, therefore, a quite subtle effect, but it is interesting that it is only observed for the simplest composition where the mixing entropy is the lowest.

3.2. Assessment of the local lattice strain

A series of simulations have recently revealed that the parameters of Gaussian peaks fitted to the PDF will be dependent on the relative scattering lengths of the constituents within the scattering system [29]. Therefore, the authors suggested that an accurate

assessment of the lattice distortion should be based on a dimensionless *strain-PDF* defined as:

$$G_{strain}(r) = \sum_{i=1}^{N} \sum_{j=1}^{N} c_i c_j \left[g_{ij}(r) - 1 \right] \tag{5}$$

This function is easily obtained from the RMC structure models. Fig. 6(a) shows Gaussian functions fitted to the strain-PDF of TiVZrNb. Similar fits were obtained for the other alloys, and Fig. 6(c) presents the obtained FWHM for the first six coordination shells. It can be seen that the local lattice distortion, as indicated by higher FWHM, is significantly higher in TiVZrNb and TiVZrNbHf in comparison to TiVNb. Thus, it is confirmed that a larger δr corresponds to a higher level of local lattice distortion. A similar analysis was undertaken for the metal lattice in the corresponding deuterides using a strain-PDF containing only the metal-
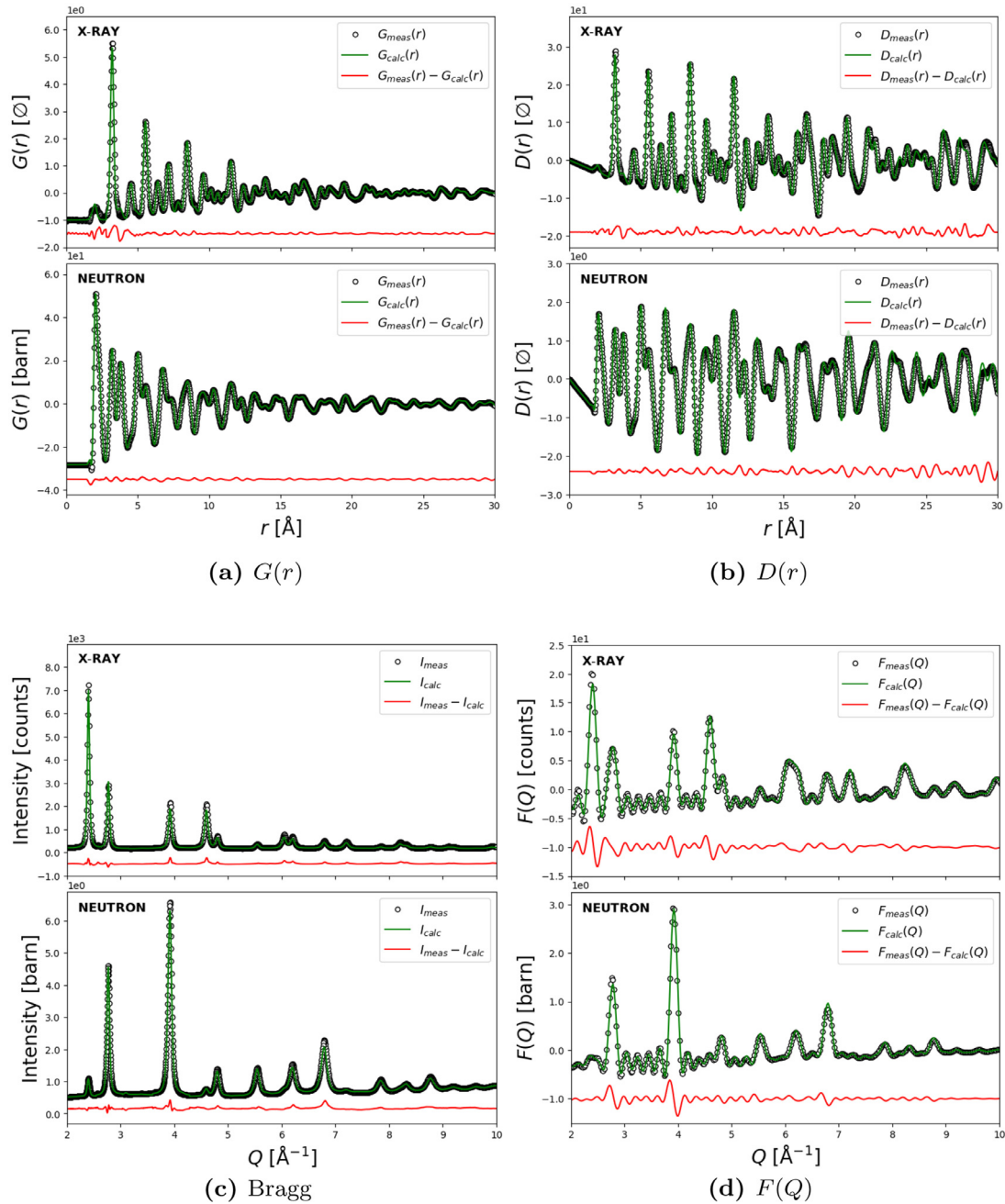
(a) $G(r)$

(b) $D(r)$

(c) Bragg

(d) $F(Q)$

Fig. 3. RMC fits to the X-ray and neutron total scattering measurements of TiVZrNbD$_8$.

metal partial PDFs. A representative fit to such a function is shown for TiVZrNbD$_8$ in Fig. 6(b), and the obtained values for the FWHM are shown for the first seven coordination shells in Fig. 6(d). It is readily seen that the trend is similar to that observed for the alloys, but the obtained values are lower. Therefore, it seems that the introduction of deuterium relieves some of the strain induced by the differently sized atoms. As a consequence, when D is desorbed from these dideuterides the level of strain is increased, and it is possible that it becomes energetically favourable for the compound to phase-separate, as it has been observed for TiVZrNbD$_8$ and TiVZrNbHfD$_{10}$ [15,16].

It should be mentioned that thermal vibrations also cause broadening of the peaks in the PDF. It is impossible to decouple the static displacements we are interested in from their dynamical counterparts in the RMC models. The mean-square displace-ments (*msd* or U_{iso}) from thermal vibrations at *RT* are typically around 0.01 Å, which yield a FWHM of around 0.24 Å in the absence of static displacements (FWHM $= 2\sqrt{2\ln(2)\cdot msd}$, assuming normal distribution). This roughly corresponds to the FWHMs observed for TiVNb in Fig. 6(c), indicating that the effect of static local lattice distortions is small compared to the thermal disorder for the ternary alloy. The FWHMs for TiVZrNb and TiVZrNbHf are significantly larger, which could be due to increased static and/or thermal displacements. The thermal vibrations in a material are related to the melting point temperature T_m. The magnitude of the vibrations are to a good approximation comparable for materials with the same homologous temperature, T/T_m. The melting point temperatures of the HEAs were estimated to 1801 °C (TiVNb), 1537 °C (TiVZrNb), and 1559 °C (TiVZrNbHf) with ThermoCalc and the TCHEA3 database, and thus similar homologous temperatures in
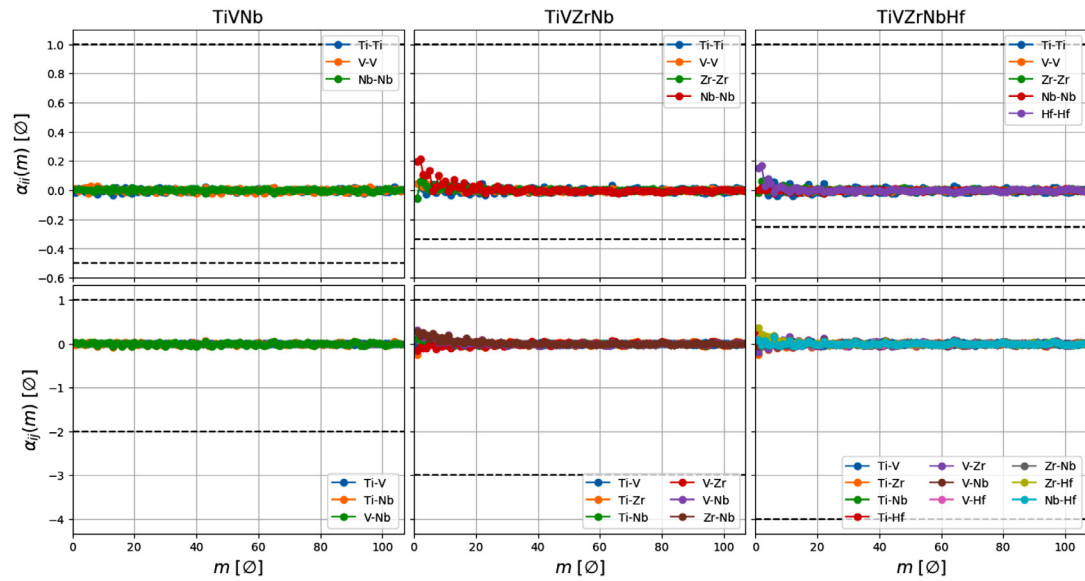
(a) Alloys.
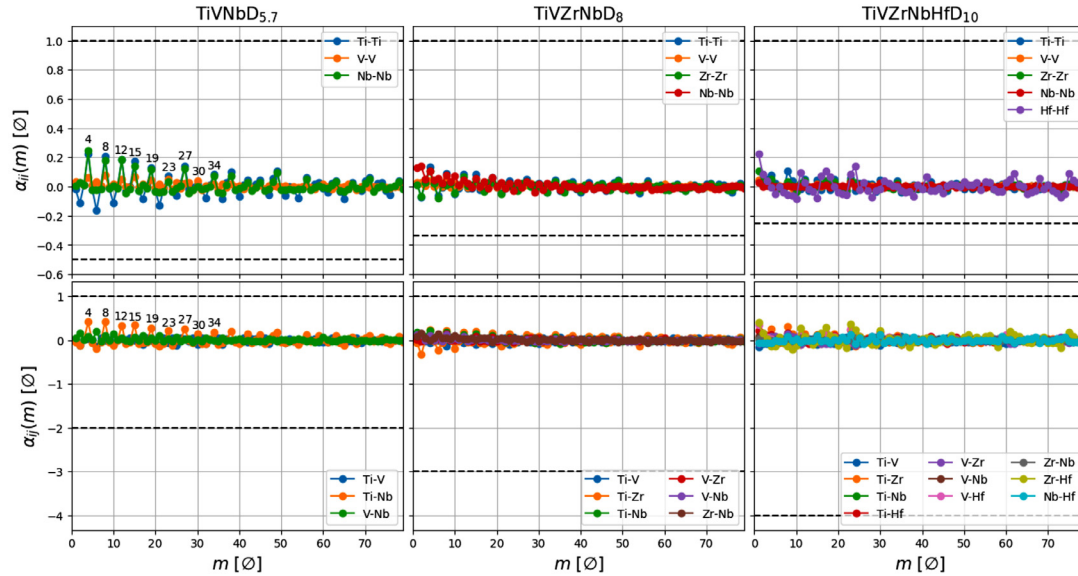
(b) Deuterides.

Fig. 4. Pairwise multicomponent short-range order (PM-SRO) parameters for the considered alloys **(a)** and the associated deuterides **(b)** extracted from the RMC structure models. The limiting values discussed in the text are indicated by dashed black lines. Coordination spheres where Ti/Nb ordering is observed are marked with numbers for TiVNbD$_{5.7}$.

the range of 0.13–0.15. Therefore, it seems likely that these HEAs have similar degree of thermal disorder and that the much larger FWHMs in TiVZrNb ($\delta r = 6.87$ %) and TiVZrNbHf ($\delta r = 6.96$ %) are due to a larger degree of static local lattice distortions.

3.3. Site preference for the D-atoms

The Rietveld refinement in Fig. 1 shows that the deuterium atoms solely occupy tetrahedral interstices in TiVZrNbD$_8$ with [D]/[M] = 2. Thus, this site is fully occupied. Furthermore, in TiVNbD$_{5.7}$ deuterium is only situated in the tetrahedral interstices, but the Rietveld refinement indicates that around 5 % of the sites are unoccupied. We have recently shown that the stability of hydrides formed from bcc HEAs decreases when the bulk

valence-electron concentration (*VEC*) of the alloy increases [16]. It is possible that this effect is present also at the local level, *i.e.*, that deuterium is desorbed from sites surrounded by elements with higher *VEC* before others. The fraction of occupied sites $N_{occupied}/N_{tot}$ with specific nearest-neighbour environments in the RMC structure model of TiVNbD$_{5.7}$ are shown in Fig. 7 as a function of the nearest-neighbours' valence-electron concentration *VEC*. Indeed, the figure clearly demonstrates that the occupied fraction is reduced when the average *VEC* of the nearest-neighbours increases. This suggests that the stability of the tetrahedral interstices with respect to deuterium occupation are directly correlated to the average *VEC* of the four coordinating metal atoms. It is not possible to establish a similar relationship for TiVZrNbD$_8$ since there are no vacant tetrahedral sites, and thus $N_{occupied}/N_{tot} = 1$
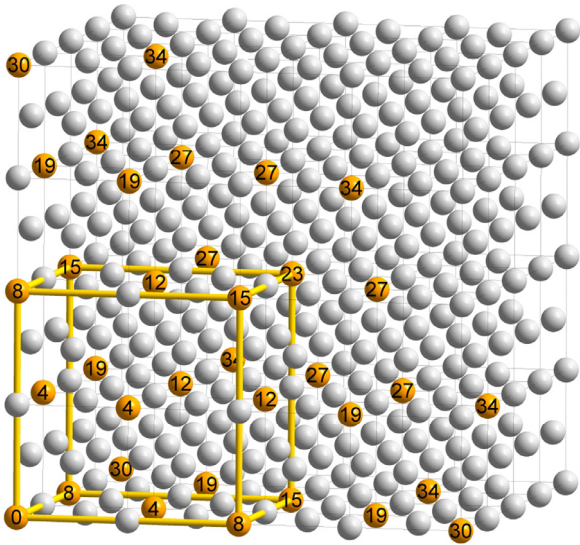
Fig. 5. $4 \times 4 \times 4$ face-centered cubic unit cells. The orange atoms are located in co-ordination spheres where there is increased probability of finding Nb around a Nb atom or Ti around a Ti atom according to the RMC structure model of TiVNbD$_{5.7}$, *i.e.*, coordination sphere 4, 8, 12, 15, 19, 23, 27, 30 and 34. These sites form a $2 \times 2 \times 2$ supercell, and one such supercell is outlined with thicker, orange lines. The numbers on the orange atoms indicate the coordination sphere numbers relative to atom marked "0" in the bottom left corner.
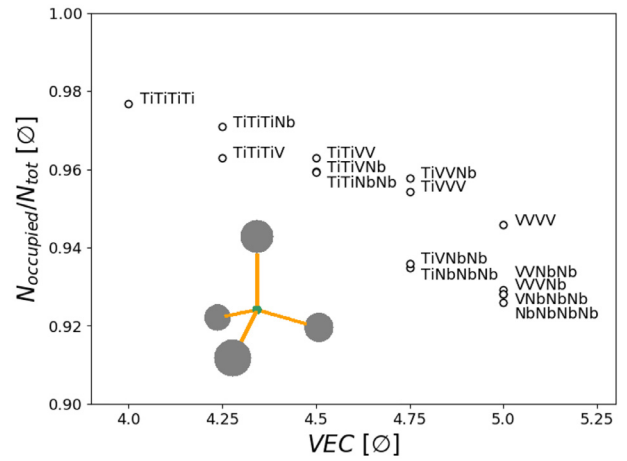

Fig. 7. The fraction of tetrahedral environments that are occupied by D in the RMC structure model of TiVNbD$_{5.7}$ as a function of the valence-electron concentration *VEC* of the four nearest neighbour metals. The inset shows a tetrahedron formed by four metals (grey spheres) surrounding a central D atom (green sphere) for reference.
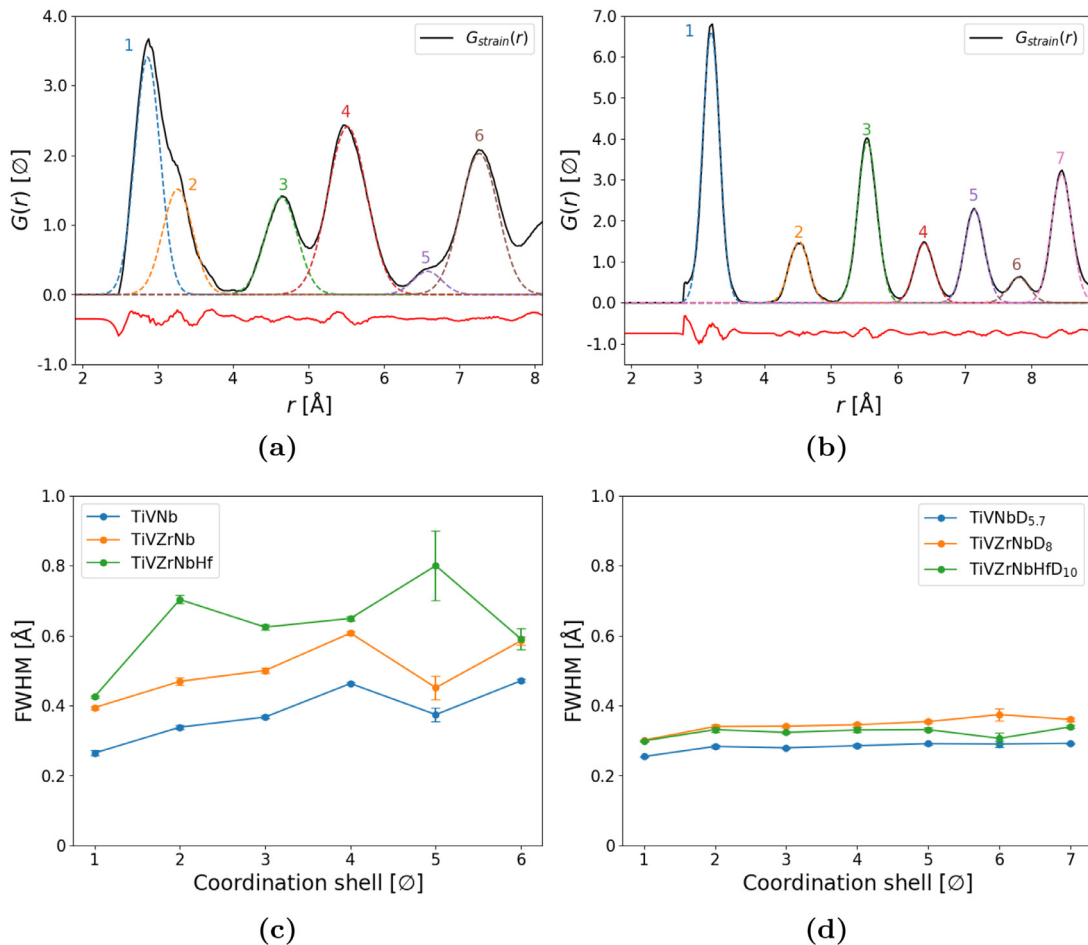

Fig. 6. Gaussian peaks fitted to metal-only strain-PDFs of TiVZrNb **(a)** and TiVZrNbD$_8$ **(b)**. Corresponding fits were obtained for TiVNb, TiVZrNbHf and their corresponding deuterides. The full-widths at half maximum (FWHM) from these fits are shown as a function of coordination shell for the alloys and deuterides in **(c)** and **(d)**, respectively.
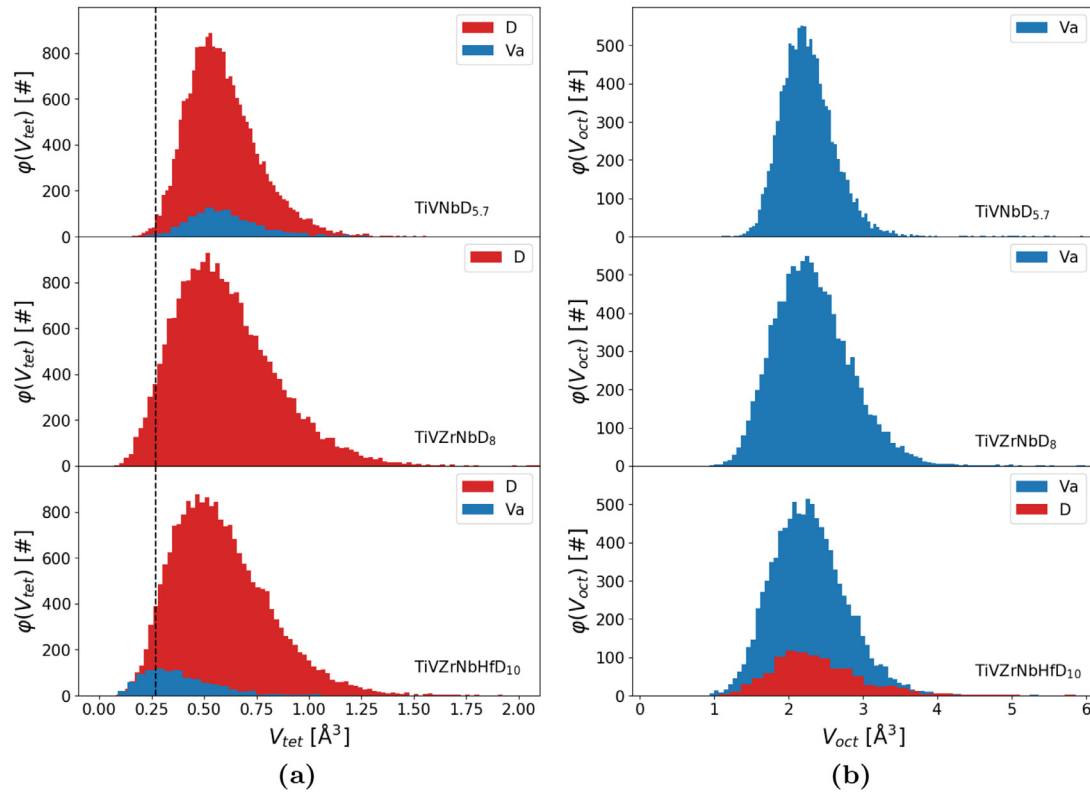
Fig. 8. The distribution of tetrahedral ($\varphi(V_{tet})$) **(a)** and octahedral ($\varphi(V_{oct})$) **(b)** interstitial volumes that are vacant (Va) and occupied by deuterium (D) in the RMC structure models of TiVNbD$_{5.7}$, TiVZrNbD$_8$ and TiVZrNbHfD$_{10}$. The dashed line indicates the Westlake criterion.

for all nearest-neighbour environments. The full D-occupancy in TiVZrNb as opposed to the slight deuterium deficiency in TiVNb can be due to the higher *VEC* of the latter (4.67 vs. 4.50).

Furthermore, in TiVZrNbHfD$_{10}$ the Rietveld refinement indicates that the tetrahedral interstices are only partially occupied. However, in this case the remaining deuterium atoms are not desorbed from the structure, but rather occupy 12 % of the octahedral interstices. A very high hydrogen content of [H]/[M] = 2.5 has been reported for TiVZrNbHfH$_x$ [13]. It might be possible to achieve this in other HEAs if the mechanism that enables the simultaneous occupation of both octahedral and tetrahedral interstices is understood. In this context, there are two important criteria that must be met to enable hydrogen to occupy an interstitial site. Firstly, *the Switendick criterion* states that the minimum distance between two hydrogen atoms should on average be larger than 2 Å [30]. Secondly, *the Westlake criterion* dictates that an interstitial volume should be large enough to accomodate a sphere with radius 0.4 Å ($V = 0.268$ Å^3) in order to be accessible for hydrogen/deuterium [31,32]. These criteria are rarely violated [33].

In the present work the interstitial volumes that are occupied by hydrogen are calculated as described by Algorithm 1 in the supplementary information. The results of these calculations are shown in Fig. 8 for sites that are vacant and occupied by deuterium in the RMC structure models, respectively. In general, most of the D-occupied interstitial volumes are larger than the Westlake criterion. For TiVNbD$_{5.7}$ both the occupied and vacant distributions are centered at the same value. This indicates that the size of the tetrahedral interstices have no influence on the stability of the tetrahedral sites with respect to deuterium occupation. Thus, the destabilization mechanism discussed above is solely due to the *VEC*. For TiVZrNbHfD$_{10}$ the distribution of vacant tetrahedral interstitial volumes are shifted towards smaller volumes in the distribution. This indicates a tendency for deuterium atoms

to avoid occupying smaller interstitial volumes, *i.e.*, surrounded by larger elements such as Zr and Hf. It is reassuring that the distribution is centered at the Westlake criterion, but there are still some sites with volumes smaller than 0.268 Å^3 that are occupied by deuterium. Nevertheless, the Westlake criterion was developed for crystallographic average structures and, therefore, some deviations are expected in a RMC structure model that reflects static and dynamic atomic displacements. Fig. 8 also demonstrates that the octahedral interstitial volumes that are vacant and occupied by deuterium in the RMC structure model of TiVZrNbHfD$_{10}$ are centered on the same value. Thus, the displaced deuterium atoms do not favour either smaller or larger octahedral volumes. The distribution of volumes for TiVZrNbHfD$_{10}$ is comparable to that of TiVZrNbD$_8$ for which there is no occupancy of octahedral interstices. The interstitial volumes are, therefore, unable to explain why certain octahedral interstices are preferred over others in TiVZrNbHfD$_{10}$ and why there is no occupancy of the octahedral interstices in TiVZrNbD$_8$. Nevertheless, there is a clear indication that deuterium atoms tend to avoid occupation of smaller tetrahedral volumes in TiVZrNbHfD$_{10}$ in accordance with the Westlake criterion.

Several attempts have been made to identify the mechanism that enable the simultaneous occupation of octahedral and tetrahedral interstices in TiVZrNbHfD$_{10}$. Unfortunately, no correlation has been determined with any reasonable parameter, *i.e.*, δr, VEC, concentrations of different elements among the nearest neighbour metals, *etc*. Finally we consider the *Switendick criterion*. The distance between a pair of adjacent tetrahedral and octahedral interstices in a face-centered cubic lattice with lattice parameter a is given by $d = \sqrt{3}/4 \cdot a$. Using the lattice parameters in Table 3, we find that $d = 1.92$ Å, $d = 1.96$ Å and $d = 1.98$ Å in TiVNbD$_{5.7}$, TiVZrNbD$_8$ and TiVZrNbHfD$_{10}$, respectively. Even though the difference is small between the three materials, it could explain

why deuterium occuapion of octahedral interstices is possible in TiVZrNbHf and not in the two other compounds.

4. Conclusions

The present work has explored the average and local structure of TiVNb, TiVZrNb and TiVZrNbHf as well as their associated deuterides with total scattering measurements and RMC structure modelling. The alloys form bcc crystal structures ($Im\overline{3}m$) where the metals are distributed over a single crystallographic site with almost complete homogeneity at the atomic level. The corresponding deuterides form CaF_2-type structures ($Fm\overline{3}m$). There is a tendency towards short-range order in TiVNbD$_{5.7}$ where Ti and Nb form $2 \times 2 \times 2$ face-centered cubic supercells. The deuterium atoms solely occupy tetrahedral interstices in TiVNbD$_{5.7}$ and TiVZrNbD$_8$. ~ 5 % of the tetrahedral interstices are unoccupied in TiVNbD$_{5.7}$, and the probability for a site to be unoccupied increases with the average VEC of the nearest-neighbour metals. Thus, the stability of the tetrahedral interstices with respect to deuterium occupation are directly correlated to the average VEC of the four coordinating metals. In TiVZrNbHfD$_{10}$, 94 % of the tetrahedral interstices and 12 % of the octahedral interstices are occupied. Analysis of the RMC structure model indicates that there is a tendency for D to avoid occupation of smaller, tetrahedral interstitial volumes. Instead, these D atoms are displaced to octahedral interstices.

The amount of lattice distortion in the alloys and deuterides has also been evaluated by analyzing strain-PDFs obtained from the RMC structure models. Our analysis indicates that the lattice becomes increasingly distorted when the spread in atomic sizes is increased. For instance, the values obtained for the HEA TiVZrNbHf ($\delta r = 6.96$ %) are on average almost twice as large as those obtained for TiVNb ($\delta r = 4.29$ %). We also observe that the level of distortion is significantly reduced when deuterium is incorporated into the structure. This is proposed as a possible explanation to why TiVZrNbD$_8$ and TiVZrNbHfD$_{10}$ phase separates when deuterium is desorbed from these compositions.

Declaration of Competing Interest

The authors declare that they have no known competing financial interests or personal relationships that could have appeared to influence the work reported in this paper.

Acknowledgements

Supplementary material

Supplementary material associated with this article can be found, in the online version, at doi:10.1016/j.actamat.2020.08.045.

References

[1] M.-H. Tsai, J.-W. Yeh, High-entropy alloys: a critical review, Mater. Res. Lett. 2 (3) (2014) 107–123.

[2] D. Miracle, O. Senkov, A critical review of high entropy alloys and related concepts, Acta Mater. 122 (2017) 448–511.

[3] E.P. George, D. Raabe, R.O. Ritchie, High-entropy alloys, Nat. Rev. Mater. 4 (8) (2019) 515–534.

[4] E. Pickering, N. Jones, High-entropy alloys: a critical assessment of their founding principles and future prospects, Int. Mater. Rev. 61 (3) (2016) 183–202.

[5] S. Froyen, C. Herring, Distribution of interatomic spacings in random alloys, J. Appl. Phys. 52 (12) (1981) 7165–7173.

[6] I. Toda-Caraballo, J. Wróbel, S. Dudarev, D. Nguyen-Manh, P. Rivera-Díaz-del Castillo, Interatomic spacing distribution in multicomponent alloys, Acta Mater. 97 (2015) 156–169.

[7] Y. Jien-Wei, Recent progress in high entropy alloys, Annales de Chimie – Science des Matériaux 31 (6) (2006) 633–648.

[8] J.-W. Yeh, Physical metallurgy of high-entropy alloys, JOM 67 (10) (2015) 2254–2261.

[9] L.R. Owen, N.G. Jones, Lattice distortions in high-entropy alloys, J. Mater. Res. 33 (19) (2018) 2954–2969.

[10] W. Guo, W. Dmowski, J.-Y. Noh, P. Rack, P.K. Liaw, T. Egami, Local atomic structure of a high-entropy alloy: an X-ray and neutron scattering study, Metall. Mater. Trans. A 44 (5) (2013) 1994–1997.

[11] Y. Tong, S. Zhao, H. Bei, T. Egami, Y. Zhang, F. Zhang, Severe local lattice distortion in Zr-and/or Hf-containing refractory multi-principal element alloys, Acta Mater. 183 (2020) 172–181.

[12] L. Owen, E. Pickering, H. Playford, H. Stone, M. Tucker, N. Jones, An assessment of the lattice strain in the CrMnFeCoNi high-entropy alloy, Acta Mater. 122 (2017) 11–18.

[13] M. Sahlberg, D. Karlsson, C. Zlotea, U. Jansson, Superior hydrogen storage in high entropy alloys, Sci. Rep. 6 (2016) 36770.

[14] D. Karlsson, G. Ek, J. Cedervall, C. Zlotea, K.T. Møller, T.C. Hansen, J. Bednarcik, M. Paskevicius, M.H. Sørby, T.R. Jensen, U. Jansson, M. Sahlberg, Structure and hydrogenation properties of a HfNbTiVZr high-entropy alloy, Inorg. Chem. 57 (4) (2018) 2103–2110.

[15] M.M. Nygård, G. Ek, D. Karlsson, M. Sahlberg, M.H. Sørby, B.C. Hauback, Hydrogen storage in high-entropy alloys with varying degree of local lattice strain, Int. J. Hydrogen Energy 44 (55) (2019) 29140–29149.

[16] M.M. Nygård, G. Ek, D. Karlsson, M.H. Sørby, M. Sahlberg, B.C. Hauback, Counting electrons – a new approach to tailor the hydrogen sorption properties of high-entropy alloys, Acta Mater. 175 (2019) 121–129.

[17] P.M. Abdala, H. Mauroy, W. Van Beek, A large-area CMOS detector for high-energy synchrotron powder diffraction and total scattering experiments, J. Appl. Crystallogr. 47 (1) (2014) 449–457.

[18] A.K. Soper, GudrunN and GudrunX: Programs for Correcting Raw Neutron and X-ray Diffraction Data to Differential Scattering Cross Section, Science & Technology Facilities Council Swindon, UK, 2011.

[19] D.A. Keen, A comparison of various commonly used correlation functions for describing total scattering, J. Appl. Crystallogr. 34 (2) (2001) 172–177.

[20] A.C. Hannon, Results on disordered materials from the GEneral Materials diffractometer, GEM, at ISIS, Nucl. Instrum. Methods Phys. Res.Sect. A 551 (1) (2005) 88–107.

[21] O. Arnold, J.-C. Bilheux, J. Borreguero, A. Buts, S.I. Campbell, L. Chapon, M. Doucet, N. Draper, R.F. Leal, M. Gigg, V. Lynch, A. Markvardsen, D. Mikkelson, R. Mikkelson, R. Miller, K. Palmen, P. Parker, G. Passos, T. Perring, P. Peterson, S. Ren, M. Reuter, A. Savici, J. Taylor, R. Taylor, R. Tolechenov, W. Zhou, J. Zikovsky, Mantiddata analysis and visualization package for neutron scattering and μ SR experiments, Nucl. Instrum. Methods Phys. Res.Sect. A 764 (2014) 156–166.

[22] M.G. Tucker, D.A. Keen, M.T. Dove, A.L. Goodwin, Q. Hui, RMCProfile: reverse Monte Carlo for polycrystalline materials, J. Phys. 19 (33) (2007) 335218.

[23] A.C. Larson, R.B. Von Dreele, General Structure Analysis System (GSAS), Los Alamos National Laboratory Report LAUR 86–748, 1994.

[24] B.H. Toby, EXPGUI, a graphical user interface for GSAS, J. Appl. Crystallogr. 34 (2) (2001) 210–213.

[25] P. Thompson, D. Cox, J. Hastings, Rietveld refinement of Debye–Scherrer synchrotron X-ray data from Al2O3, J. Appl. Crystallogr. 20 (2) (1987) 79–83.

[26] S. Ikeda, J.M. Carpenter, Wide-energy-range, high-resolution measurements of neutron pulse shapes of polyethylene moderators, Nucl. Instrum. Methods Phys. Res.Sect. A 239 (3) (1985) 536–544.

[27] V.F. Sears, Neutron scattering lengths and cross sections, Neutron News 3 (3) (1992) 26–37.

[28] D. de Fontaine, The number of independent pair-correlation functions in multicomponent systems, J. Appl. Crystallogr. 4 (1) (1971) 15–19.

[29] L. Owen, H. Stone, H. Playford, The assessment of local lattice strains in alloys using total scattering, Acta Mater. 170 (2019) 38–49.

[30] B. Rao, P. Jena, Switendick criterion for stable hydrides, Phys. Rev. B 31 (10) (1985) 6726.

[31] D. Westlake, Site occupancies and stoichiometries in hydrides of intermetallic compounds: geometric considerations, J. Less Common Metals 90 (2) (1983) 251–273.

[32] D. Westlake, Hydrides of intermetallic compounds: a review of stabilities, stoichiometries and preferred hydrogen sites, J. Less Common Metals 91 (1) (1983) 1–20.

[33] V. Yartys, R. Denys, B. Hauback, H. Fjellvåg, I. Bulyk, A. Riabov, Y.M. Kalychak, Short hydrogen–hydrogen separations in novel intermetallic hydrides, RE3Ni3In3D4 (RE = La, Ce and Nd), J. Alloys Compd. 330 (2002) 132–140.